Available online at www.sciencedirect.com
SCIENCE DIRECT®
Journal of Power Sources 125 (2004) 155–165
JOURNAL OF POWER SOURCES
www.elsevier.com/locate/jpowsour

Design, assembly and operation of polymer electrolyte membrane fuel cell stacks to 1 kW_e capacity

S. Giddey*, F.T. Ciacchi, S.P.S. Badwal

CSIRO Manufacturing and Infrastructure Technology, Private Bag 33, Clayton South, 3169 Vic., Australia

Received 14 July 2003; accepted 6 August 2003

Abstract

Polymer electrolyte membrane (PEM) fuel cell stacks to 1 kW_e capacity, with an active area of 225 cm^2 per cell, have been constructed and operated to investigate the fuel quality issues (one of the major barriers for commercialization of this technology), and start/stop, thermal cycling and load following capabilities. The stacks were assembled and tested in stages of 2-, 4-, 8- and 15-cell configurations. This paper describes the design and assembly of the stacks tested, analysis of the results and problems encountered during operation. Though the 1 kW_e stack showed a large variation in the temperature of the interconnect plates due to uneven cooling, the individual cell voltages were found to be within 86 mV (under full load). The average power produced by each cell for the 1 kW_e stack operating on air/H_2 was 67.5 W (300 mW cm^{-2}). The stack has undergone more than 40 cold start/shut down thermal cycles in the power output range of 0.6–1 kW_e over an accumulated operation of ~300 h with a small degradation in its performance. The electrical efficiency of the stack varied from 39 to 41%. The recoverable combined heat and power (CHP) efficiency of the stack was 65% without external thermal insulation and 80% with external thermal insulation.

Keywords: Polymer electrolyte membrane fuel cell; Fuel cell stack; Distributed energy generation

1. Introduction

The distributed energy generation has progressed well beyond the concept stage and becoming more of a reality following the deregulation of the power industry and the increasing availability of emerging efficient and environmentally friendly technologies such as fuel cells and renewable energy technologies. Co-generation (heat and electricity) or tri-generation (heating, cooling, electricity) at distributed or load centres inherently offer higher efficiencies compared to centralized power generation. Fuel cells are ideal candidates for distributed power generation due to their high efficiency, low chemical and particulate matter emissions, the ability to co-generate heat and electricity (the quality of heat depending on the type of fuel cell and the operating temperature), and fast response to changing electric loads [1]. The major problems facing fuel cell technology are cost and reliability (life time and degradation for different end user applications—transport, stationary, portable power, etc.) and hence user comfort. Although, the fuel cell costs of early commercial (phosphoric acid) or demonstration (polymer electrolyte membrane (PEM), solid oxide and molten carbonate) units at present are high, detailed cost analysis for the main subsystems indicates that prices will be driven down to the required levels through technology refinement and increasing production volumes [2].

Polymer electrolyte membrane fuel cells operate at low temperatures (60–80 °C), offer a fast start-up and shut down time (few minutes), fast response to changing electric loads, and can sustain unlimited thermal cycles. They are ideally suited for transport, small stationary and portable power applications. PEM fuel cell stacks operating on hydrogen can produce over 45–50% electrical efficiency with system efficiencies (with heat recovery) exceeding 80%. The size of a PEM fuel cell system can vary from less than 100 W for most portable power applications to few kW_e (stationary-residential or small transport vehicles), 50–75 kW_e for cars and 200–250 kW_e for buses and trucks.

PEM fuel cells are susceptible to degradation in their performance with time due to several reasons. For example, the presence of CO in the hydrogen fuel above 10 ppm levels leads to catalyst poisoning. Major sources of hydrogen for PEM fuel cell are fossil fuels (reforming of natural gas, gasoline, partial oxidation of methanol or coal gasification)

* Corresponding author. Tel.: +61-3-9545-2777; fax: +61-3-9544-1128.
E-mail address: sarb.giddey@csiro.au (S. Giddey).

0378-7753/$ – see front matter © 2003 Published by Elsevier B.V.
doi:10.1016/j.jpowsour.2003.08.026

and water (electrolysis using renewable energy). The latter route although offering totally sustainable energy cycle and clean source of hydrogen, is not cost effective at this stage due to the high cost of renewable energy technologies. Most hydrogen is produced from natural gas (comprising of processes such as pre-cleaning to remove sulphur compounds, steam reforming and/or partial oxidation to produce a mixture of $CO + H_2$ followed by water gas shift reaction to convert CO to H_2 and CO_2). The product mixture usually consists of 80% H_2, 18–20% CO_2, up to 0.1% CO, and residual methane and water. Further processing is required to reduce CO and/or CO_2 levels acceptable for use in PEM fuel cells. Cell degradation can also occur due to contamination of (from fuel, air and humidifying water), and dimensional changes in the polymer electrolyte membrane. The contamination and drying of the membrane can result in poor efficiency of proton transport from anode to cathode, and the dimensional changes in membrane may also cause stresses at electrode/membrane interfaces and gaskets, electrode de-bonding from membrane and buckling of carbon paper due to membrane shrinkage. The electrode support (i.e. carbon paper backing) is also prone to degradation due to buckling and cracking from stack assembly stresses, changes in hydrophobic properties, and damage to the porous structure resulting in poor conductivity and gas/water diffusion. The corrosion/oxidation of interconnect (metallic) and current collector plates can increase contact resistances resulting in higher voltage losses.

In the present study, PEM fuel cell stacks up to 1 kW electric power output (15 cells) were designed and assembled to study the start, stop, thermal cycling, load following capability and fuel quality issues. This paper describes the design of the stack and the test results obtained. The stack was built in-house to better understand the functionality and performance of the stack.

2. Stack design and assembly

2.1. Membrane electrode assembly

A three layer structure consisting of diffusion, catalyst and ionomer layers was used to prepare the electrodes [3,4] of the membrane electrode assemblies (MEAs). Each MEA had an active area of 225 cm^2 (150 mm × 150 mm). A TGPH-120 Toray carbon paper of thickness 0.35 mm was used as a backing layer for the electrodes. The diffusion ink for the diffusion layer was prepared from Vulcan XC72R carbon powder, PTFE solution and butyl acetate as the solvent. The diffusion layer was prepared by coating the diffusion ink on the carbon paper followed by drying. The catalyst ink for the catalyst layer was prepared from 20 wt.% Pt dispersed on carbon, 5 wt.% Nafion solution and butyl acetate as the solvent. The catalyst layer was prepared by screen-printing the catalyst ink on top of the diffusion layer followed by drying in a vacuum oven. The catalyst loading

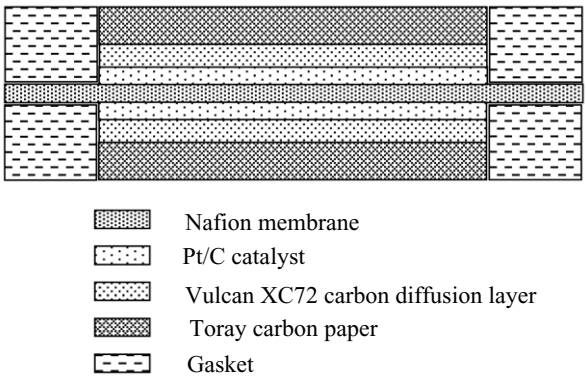

Fig. 1. A schematic view of the components of a membrane electrode assembly.

was 0.4–0.5 mg cm^{-2} Pt in a total catalyst layer thickness in the range of 40–50 μm. The polymer electrolyte membrane used was Nafion 112 (Dupont Fluoro Products). The membrane was purified by treating with H_2O_2 and H_2SO_4 according to the procedure given in the literature [5]. The membrane electrode assembly was prepared by hot pressing the air electrode–polymer membrane–fuel electrode layers. Fig. 1 shows a schematic view of the membrane electrode assembly along with the gaskets for sealing on both sides of the membrane.

2.2. Interconnect and current collector plates

The interconnect plates, each of cross-section 190 mm × 190 mm were fabricated from graphite material procured from UCAR Carbon Company Inc. For the 1 kW_e stack, 15 MEAs required 15 hydrogen flow fields and 15 air flow fields, and 6 water cooling interfaces evenly distributed among the 15 MEAs along the length of the stack.

Hydrogen and air flow fields consisted of a serpentine pattern of parallel multi-channels and ribs in a cross-sectional area of 151 mm × 151 mm. Water cooling flow field consisted of two sets of single channel serpentine flow field of channels and ribs in a cross-sectional area of 138 mm × 142 mm. Fig. 2 shows the schematic view of the internal hydrogen, air and cooling water flow circuit of the stack. The cooling water interface, at both ends of the stack, was formed between the current collector plate and an interconnect plate having a water flow field on one side and a hydrogen or air flow field on the other side. The cooling water interface in between the stack was formed between two interconnect plates having water flow fields opposing each other. In order to prevent any leakage of gases (and cooling water) from one compartment to the other (hydrogen, air and cooling water compartments) or to atmosphere, gaskets were used between various interfaces in the stack assembly. The current collection was performed by nickel plated copper plates in contact with the water cooling flow field sides of the outer interconnect plates of the stack.

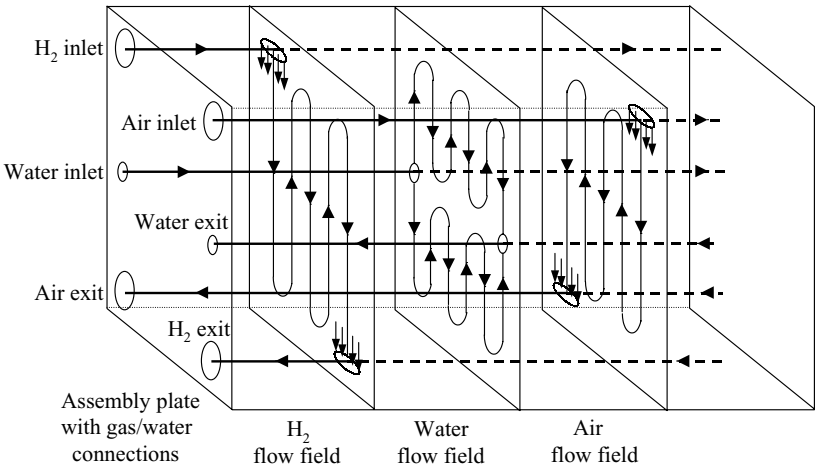

Fig. 2. A schematic view of the internal hydrogen, air and cooling water flow circuit of the CMIT stack.

2.3. Stack assembly

The MEAs with interconnect plates, water cooling plates and current collector plates were stacked and assembled with the help of square aluminium plates and eight 'all threaded' tie rods. Belleville spring washers were used on both sides of the tie rods and the stack was tightened to a maximum torque of 30 N m. The stack was assembled in stages as a 2-, 4-, 9- and 15-cell stack as shown in Fig. 3.

2.4. Stack electrical insulation and gas leakage test

The stack was tested for electrical short-circuiting by measuring resistance between different components of the stack, i.e. between current collector plates (positive and negative), between current collector plates and stack assembly plates, between current collector plates and interconnect plates, or between individual interconnect plates.

Nitrogen gas was used to test the gas leakage from hydrogen, air and cooling water compartments, and cross leak-

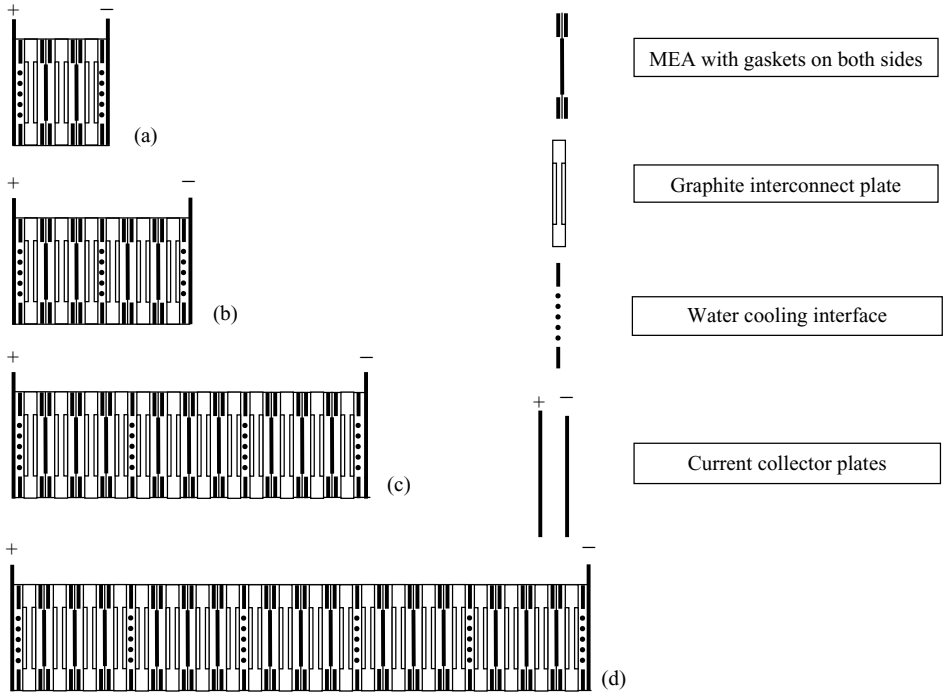

Fig. 3. A schematic view of various configurations of 225 cm^2 active area stacks: (a) 2-cell; (b) 4-cell; (c) 9-cell; and (d) 15-cell.

age from one compartment to the other. Each compartment was tested individually by pressurizing to 1.3 bar A and observing a drop in the pressure when the gas supply to the compartment was turned off. The cross leakage was tested from one compartment to the other by maintaining the pressure in one compartment and observing the gas leaking, if any from other compartment by connecting it to a gas bubbler.

3. Stack testing and evaluation

3.1. Test equipment and operating procedure

A test facility was established to study start, stop, thermal cycling, load following capability and fuel quality issues of PEM fuel cell stacks up to 3 kW_e capacity. The facility has been previously described in [6]. In summary, it is extremely flexible and enables the testing and evaluation of a wide range of PEM fuel cell stacks with different thermal load, electrical load, water management and humidification requirements. It has multiple levels of power and safety back-ups and has been certified as a stand alone safe gas appliance by the Australian Gas Association. In the present study a 700 W (0.4–10 V, 0–100 A) and a 2 kW (3–20 V, 0–200 A) electronic load were used for testing various stacks. The 15 cell stack was also tested with a 1 kW lighting load consisting of 24, 60 W output (12 V) globes connected in parallel. Industrial grade hydrogen was used as the fuel. The air was supplied from an in-house laboratory supply line after filtration to remove water and traces of oil. The hydrogen and air pressure regulators at the test station were set at 2 and 3 bar G, respectively. The gases were humidified at room temperature (22–25 °C) and were supplied to stacks operating in a flow through mode. However, provision existed for stacks to be operated in a dead end mode (no gas flow exiting the stack but H_2 supplied to the stack at a positive pressure). The stack cooling water was also supplied in a once through mode at room temperature (22–25 °C).

The standard test procedure for a typical run is described below. The complete flow circuit including the stack is initially purged with nitrogen. Hydrogen and air are then supplied at small flow rates for a few minutes to achieve a stable open circuit voltage (OCV) of the stack. The stack is usually loaded in steps of 5 or 10 A. The flow rates of gases are kept between one to two times the stoichiometric amount of hydrogen and three to five times the stoichiometric amount of air for all currents. The stack cooling water flow rate is controlled in such a way that the stack temperature (exit temperature of cooling water) does not exceed 65 °C. As the stack is loaded to higher values of current, at any stage, its voltage is never allowed to drop below 8 V (0.53 V per cell). Once a steady operation of the stack was achieved, the voltage–current (*V–I*) characteristics of the stack under these operating conditions were recorded. As a deviation from the above procedure, the 15 cell (1 kW_e) stack was often loaded to above 500–600 W load at the operating temperature of 22–25 °C, within a few seconds following entry of air and hydrogen fuel into the stack. This was usually done to demonstrate the flexibility of the stack operation and its capability to respond rapidly to changing loads. For this purpose a lighting panel load described previously was used as the electrical load. The stack response to rapidly switching lights on and off was found to be almost instantaneous in terms of increase or decrease in stack voltage, without causing any instability in the stack performance.

3.2. Operating parameters and polarization curves

The different configurations of the 225 cm^2 active area stacks shown in Fig. 3 were tested. Table 1 shows the operating and calculated performance parameters of different size stacks. None of these stacks had external thermal insulation. In the case of a nine-cell stack, one of the end cells had

Table 1
Operating and calculated parameters of the CMIT in-house built PEM fuel cell stacks of different sizes

Parameter	2-Cell stack	4-Cell stack	8-Cell stack	15-Cell stack
H_2 flow rate ($l\,min^{-1}$)	2.8	5.5	8.8	16.2
Air flow rate ($l\,min^{-1}$)	22.4	25.2	64.3	113.4
H_2 back pressure (bar A)	1.30	1.65	1.55	1.60
Air back pressure (bar A)	1.50	1.65	1.65	1.70
Cooling water flow rate ($ml\,min^{-1}$)	47	68	142	247
Temperature (°C)	60	60	57	60
Current (max) (A)	140	130	130	125
H_2 stoichiometric factor	1.43	1.52	1.21	1.2
Air stoichiometric factor	4.82	2.92	3.73	4.25
Maximum power output (W)	140	295	530	1011
Power output per cell (W)	70	73.7	66.2	67.4
E_0 (V)	1.010	1.017	0.990	0.987
b (mV per decade)	122.7	102.7	92.1	85.9
R ($\Omega\,cm^2$)	0.251	0.228	0.338	0.328
Correlation coefficient	0.997	0.999	0.999	0.999

Humidifiers of H_2 and air were at room temperature. Cooling water was fed to the stacks at room temperature in a once flow through mode.

been damaged while assembling the stack and was shorted. Therefore, the results given in the paper are essentially for an eight-cell stack. The operating temperature of the stacks given in the table was measured at the exit port of the cooling water sub-circuit. The surface temperatures of individual interconnect plates were also measured and a large variation was found to exist between the plates. This probably resulted from an uneven water cooling of the interconnect plates of the stack. In the case of the 1 kW_e stack (15 cells), a temperature variation of up to 25 °C was observed across the stack. The stacks were operated at a maximum back-pressure of 1.65 bar A on the hydrogen side and 1.7 bar A on the air side. All stacks were operated between 57 and 60 °C. The hydrogen supplied to stacks was typically in the range of 1.2–1.5 times the stoichiometric value, and the air supplied was in the range of 2.9–4.8 times the stoichiometric value. The average power output obtained from each cell was in the range of 66.2–73.7 W for different stacks.

A fuel cell stack suffers from voltage losses, which primarily originate from three sources: activation polarization, ohmic polarization and concentration polarization. The activation polarization loss is dominant at low current densities and is present when the rate of an electrochemical reaction at the electrode surface is controlled by sluggish electrode kinetics. The processes involving absorption of reactant species, transfer of electrons across the double layer, desorption of product species, the number and distribution of active sites, and the nature of the electrode surface can all contribute to activation polarization. Ohmic losses vary directly with current, increasing over the entire range of current density. These are due to the resistance to the flow of protons in the electrolyte membrane and resistance to flow of electrons through the stack materials, i.e. electrode materials, electrode backing, interconnects, current collector plates and contact resistance between various interfaces [7]. The ohmic losses can be reduced by using thinner electrolyte membranes with proper humidification, better conductivity cell/stack materials, design of the flow field and current collection plates and by reducing contact resistances at various interfaces. The concentration polarization losses occur due to the mass transport limitation of reactants/products to or from the electroactive sites. These voltage losses occur over the entire range of current density, but become prominent especially at high limiting currents, when it is difficult to provide enough reactant flow to the reaction sites. The mass transport voltage losses can be reduced by making the gas distribution over the electrode surfaces more uniform (i.e. flow field design), higher porosity (interconnected pores) of the backing layer without losing conductivity, a right combination of the hydrophobic and hydrophilic properties of materials used to construct electrode layers for efficient water removal.

The performance characteristics of a fuel cell stack and the various voltage losses occurring within stack components as discussed above can be evaluated from voltage–current characteristics of the stack obtained under particular operating conditions. The *V–I* characteristics of a single cell of a fuel cell stack can be represented by the following equation:

$$E = E_0 - b \log(i) - R(i) \quad (1)$$

where E is the cell voltage under load (mV), E_0 the open circuit voltage (mV), i the current density (mA cm^{-2}), b the Tafel slope (mV per decade) and R the ohmic resistance ($\Omega\,cm^2$) of the cell. The Tafel slope represents the voltage losses due to activation polarization of both electrodes. The activation polarization losses due to oxygen reduction on the Pt catalyst are much higher than that for hydrogen oxidation. Therefore, the voltage losses due to activation polarization can be mainly attributed to the oxygen reduction reaction in the cell. The ohmic resistance of the cell as mentioned previously is due to the resistance to flow of protons in the electrolyte membrane, resistance to the flow of electrons through the stack materials and various contact resistances.

Eq. (1) holds true in the low and intermediate current density regions [8]. At high current densities when the voltage losses due to the mass transport limitation becomes dominant, the *V–I* curve departs from linearity and the above equation does not represent the entire curve. Fig. 4 shows the voltage–current (polarization) characteristics of the assembled and tested stacks. The symbols represent the actual data recorded and the lines represent the trend lines obtained by performing non-linear regression analysis on actual data points by using the above model equation. The data points where the voltage current relationship departs from linearity (last two points at higher current densities) have been ignored while performing the regression analysis to determine the values of b and R. The values of these constants and the correlation coefficient (R^2 value of the fit) for each stack are given in Table 1. The values of ohmic resistance, R of each cell in various configurations of the stack varies from 0.228 to 0.338 $\Omega\,cm^2$. The values of Tafel slope, b varies from 85.9 to 122.7 mV per decade. It is clear from the R^2 values (0.997–0.999) in the table that the model parameters determined from the fit are very closely representing the measured data. The ohmic resistance values determined for stacks constructed in the present study, hereafter defined as CMIT stacks, are within the range of values reported by other investigators [8,9]. The major factors affecting the value of Tafel slope are properties of the electrocatalyst and the cell temperature. However, humidification conditions of gases may also have a significant effect on the Tafel slope [10]. The Tafel slope values for PEM fuel cells have been reported to be in the range of 57–110 mV per decade for Pt/C catalyst, depending on the cell temperature and humidification conditions. In the present study the results on CMIT 2-, 4- and 8-cell stacks (Table 1) showed somewhat higher values for the Tafel slope. However, as it will be discussed later in the next section, after undergoing 40 cold start/shut down cycles, the CMIT 1 kW_e stack produced an average Tafel slope of 60.4 mV per decade, which is reasonably close to the values reported by other investigators [8,9].

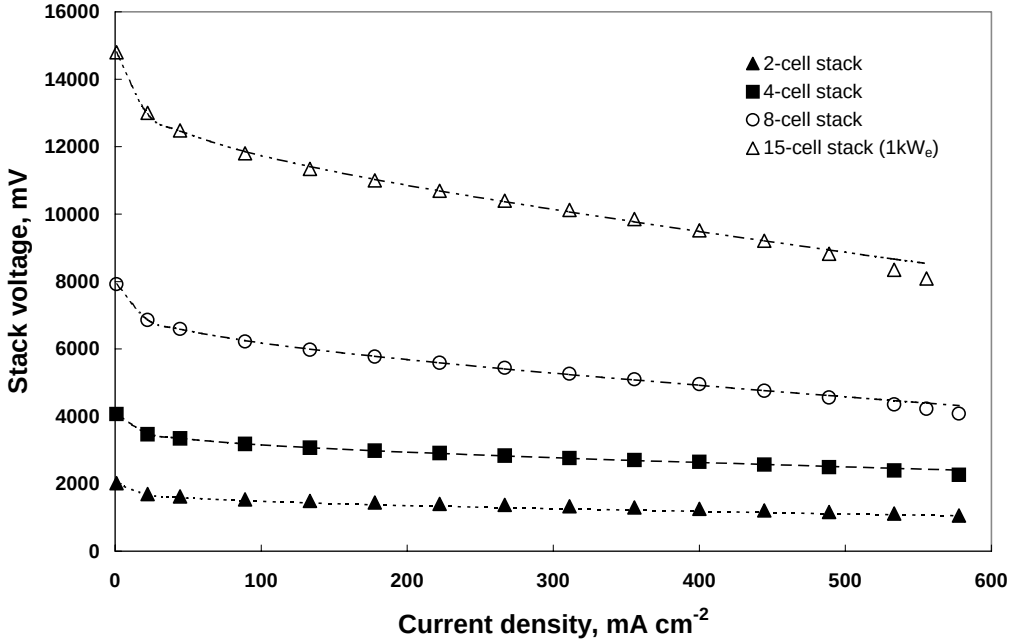

Fig. 4. *V–I* characteristics of a 2-, 4-, 8- and 15-cell (1 kW_e) stacks. The trend lines passing through the data points represent the fitted model (Eq. (1)). The operating parameters of stacks are given in Table 1.

The voltages of the individual cells of the 15 cell (the CMIT 1 kW_e) stack were monitored individually and are plotted in Fig. 5, at OCV and higher values of current loads, as a function of the cell number from the positive terminal (gas flow inlet side) of the stack. The OCV of the cells varied from 0.945 to 1.01 V. At a current load of 100 A, the cell voltages varied from 0.535 to 0.611 V. It is worth noting that irrespective of a large variation in the temperature (∼25 °C) of the interconnect plates, the variation in performance of the cells (voltage) is very small. Increasing the load from 100 to 120 A, dropped the average cell voltage from 0.57 to 0.54 V and the variation in cell voltage had only slightly gone up, i.e. from 76 mV at 100 A to 86 mV at 120 A.

3.3. Energy and mass balance

In order to assess the performance of the fuel cell stack in terms of energy efficiency, the energy input and output

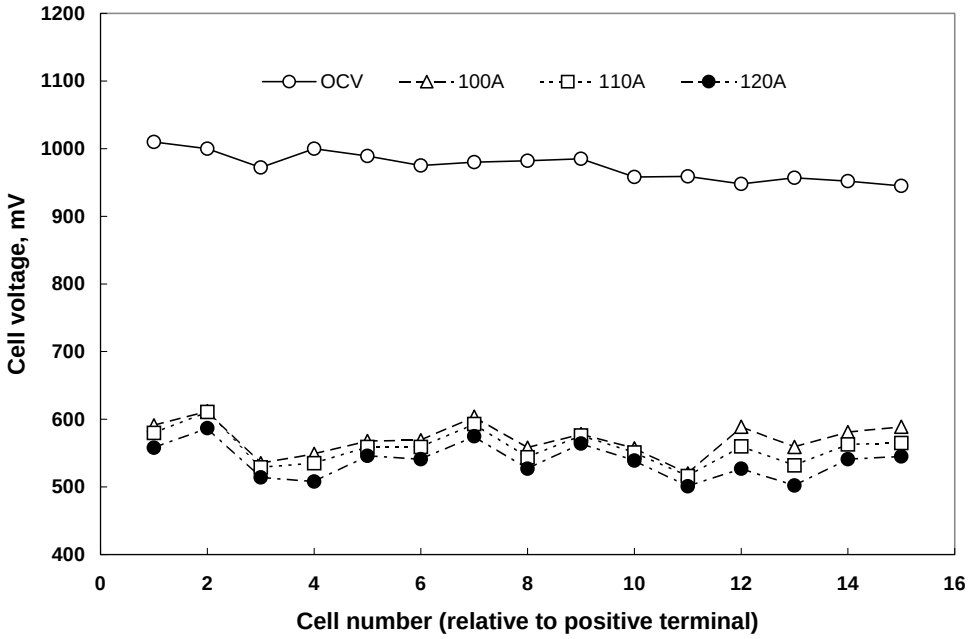

Fig. 5. Cell voltages of individual cells of CMIT 1 kW_e stack operating at different values of current load.

calculations of the stacks were made. The energy balance equation [9] for a fuel cell stack can be written as follows:

Rate of energy input
= electrical power generated
+rate of heat gained by the cooling water
+rate of heat gained by air
+rate of heat absorbed by the stack components
+rate of heat dissipated from stack external surfaces to surroundings (2)

The rate of energy input to the stack can be calculated from the volumetric flow rate of hydrogen fed to the stack. The CMIT 1 kW_e stack was operated at 1.2 times the stoichiometric amount of hydrogen as shown in Table 1. However, the stack can also be operated in dead end mode or the unspent hydrogen can be recycled to consume all the hydrogen fed to the stack. The input volumetric flow rate of hydrogen, used in the present calculations, has been assumed to be equivalent to the rate of hydrogen consumed to produce the corresponding current load. The energy output from the stack is in two forms: electrical energy output and heat output. The electrical energy output is the electrical power generated by the stack and is equal to the product of the stack voltage and the current load under particular operating conditions of the stack. The heat output consists of four components—heat gained by the cooling water, air, stack components and heat dissipated from the stack to surroundings. The rate of heat gained by the cooling water can be calculated from the rise in temperature of the cooling water fed to the stack. This component of the heat output of the stack can be very useful for residential applications of the PEM fuel cell stacks, and can increase the combined heat and power (CHP) energy efficiencies to significantly high values. The amount of water produced on the air side of the stack and the heat output component associated with that water can be assumed to be very small and therefore has not been taken into account. The rate of heat gained by air fed to the stack is also expected to be small. However, in order to calculate this component, the exit temperature of air was assumed to be the same as the cooling water exit temperature. Nevertheless, the amount of oxygen consumed in the stack was taken into consideration while performing calculations on the heat gained by air. When the current loading of the stack is started, the temperature of the stack body starts rising. The rate of heat absorbed by the stack (i.e. components) would depend upon the rate of loading of the stack and the thermal properties of the stack. Once the stack is loaded to the required value of current, and is then operated under constant operating conditions, it will attain a steady state. This will result in the rate of heat absorption by the stack components to be zero. The rate of heat dissipation from the stack surface to the surroundings would depend upon the external thermal insulation of the stack, and the surrounding air flow and temperature.

In Appendix A, all energy balance equations are given to calculate the total energy input to the stack, electrical power generated and various heat output components. The nomenclature of the terms used in these equations has also been given. The results of these calculations are shown in Table 2. The CMIT 1 kW_e stack was tested several times up to its maximum capacity in year 2001. The results shown

Table 2
Comparison of the design and operating (electrical and heat output) parameters of the CMIT 1 kW_e stack with commercial 1 kW_e stack and Ballard 5 kW_e stack

Parameter	CMIT				Commercial	Ballard
Electrical power capacity (kW)	1				1	5
Active area (cm^2)	225				225[a]	232
Number of cells	15				19	36
Experiment	Run 1	Run 2	Run 3	Run 4	–	–
Current (A)	125	110	100	100	90	175
Average cell voltage (V)	0.54	0.535	0.567	0.568	0.595	0.624
P_{elect} (kW)	1.012 (39)	0.883 (38.7)	0.851 (41.0)	0.852 (41.1)	1.017 (43.2)	4 (45)
P_{tot} (kW)	2.593	2.283	2.075	2.075	2.364	8.67
Q_w (kW)	0.689 (26.6)	0.557 (24.4)	0.817 (39.4)	0.799 (38.5)	0.875 (37.1)	3 (35)
Q_a (kW)	0.091 (3.5)	0.098 (4.3)	0.082 (3.9)	0.092 (4.4)	0.055 (2.3)	0.173 (2)
Q_{other} (kW)	0.801 (30.9)	0.745 (32.6)	0.325 (15.7)	0.332 (16.0)	0.417 (17.7)	1.5 (18)
CHP (kW)	1.701 (65.6)	1.440 (63.1)	1.668 (80.4)	1.651 (79.6)	1.892 (80.0)	7 (80.3)
E_0 (V)	0.987	0.928	0.942	0.950	0.976	1.031[b]
b (mV per decade)	85.9	58.9	61.3	61.1	58.2	69.1[b]
R ($\Omega\,cm^2$)	0.328	0.428	0.432	0.426	0.543	0.264[b]
Correlation coefficient	0.999	0.999	0.999	0.999	0.997	–

Values in parenthesis are in percentage. The CMIT stack has undergone more than 40 cold start/shutdown cycles between July 2001 and February 2003, each time operating between 600 and 800 W: run 1, without outside thermal insulation tested in August 2001; run 2, without outside thermal insulation tested in January 2003; run 3, with outside thermal insulation tested in January 2003; run 4, with outside thermal insulation tested in February 2003.

[a] Estimated from external dimensions of stack.

[b] Values at 68 °C.

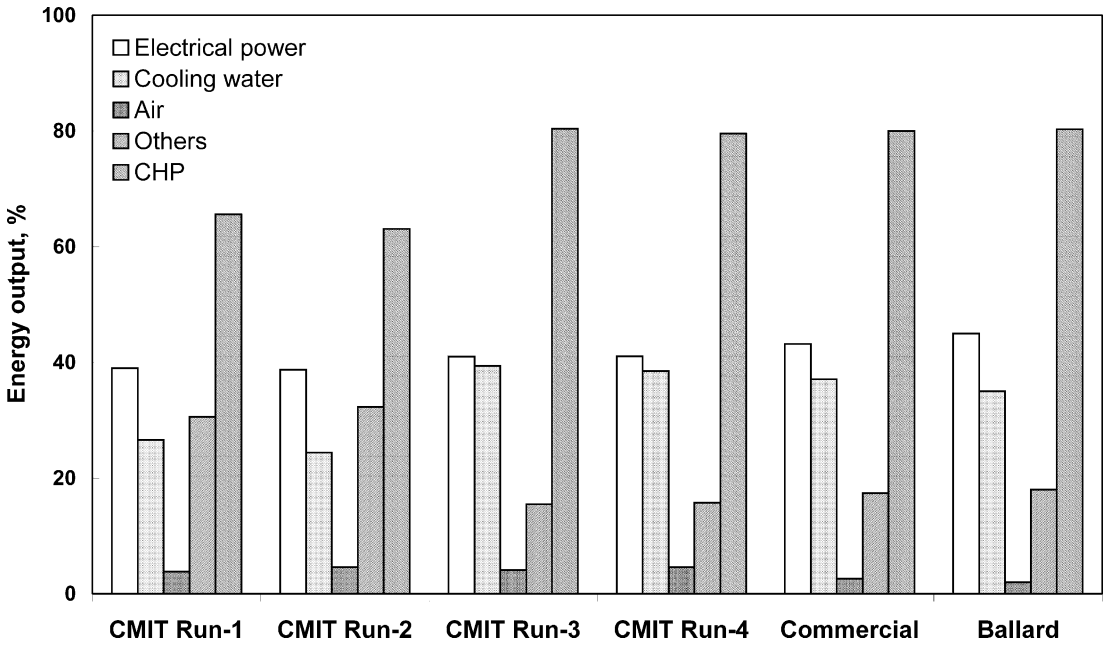

Fig. 6. Comparison of *V–I* characteristics of CMIT and commercial 1 kW_e stacks. CMIT stack: Hydrogen flow rate = 16.21 min^{-1}; air flow rate = 113.41 min^{-1}; water flow rate = 247 ml min^{-1}; stack temperature = 60 °C; H_2 back pressure = 1.6 bar A; air back pressure = 1.7 bar A. Commercial stack: Hydrogen flow rate = 131 min^{-1}; air flow rate = 64.71 min^{-1}; water flow rate = 285 ml min^{-1}; stack temperature = 64 °C; H_2 back pressure = 1.6 bar A; air back pressure = 1.5 bar A.

as run 1 are typical test results of one such test. The stack has now undergone more than 40 cold start/shut down cycles between August 2001 and January 2003, each time the stack operating between 600 and 800 W and occasionally at higher loads. The test results shown in Table 2 for runs 2–4 were obtained in January–February 2003. Runs 1 and 2 are the results of operating the stack without any external thermal insulation and runs 3 and 4 are the results of testing the stack with external thermal insulation. These results have also been plotted in Fig. 6. It can be noted that by external thermal insulation of the stack, although the electrical power generation efficiency of the stack has only increased marginally (39 to 41%), the percentage heat gained by cooling water (useful heat) has significantly increased from an average of 25.5% (runs 1 and 2) to an average of 39% (runs 3 and 4). This results in a decrease (from ∼31 to ∼15%) in the heat dissipation from the stack surface to surroundings as shown in Table 2 and Fig. 6. This data clearly indicate that by proper thermal insulation of the stack, the CHP output of the stack can be increased to more than 80%. The heat output in terms of the heat gained by the spent air exiting the stack is very low, i.e. ∼4% and thermal insulation of the stack appears to have little effect on this value.

Fig. 7 shows the voltage–current (polarization) characteristics recorded for runs 1–4 of the CMIT 1 kW_e stack. The symbols represent the actual data recorded and the lines represent the trend lines obtained by performing non-linear regression analysis on actual data points by using Eq. (1). The data points where the voltage current relationship departs from linearity (last two points at higher current densities) have been ignored while performing the regression analysis to determine the values of *b* and *R*. The values of these constants and the correlation coefficient (R^2 value of the fit) for each run are given in Table 2.

Table shows the effect of more than 40 cold start/shut down cycles of stack operation on the OCV, Tafel slope and ohmic resistance values of the stack (average of 15 cells). It can be seen in the table that OCV (E_0) value has decreased only marginally from 0.987 V (run 1 recorded at the start of the stack testing in 2001) to 0.94 V (average of runs 2–4 recorded in February 2003) with time. The Tafel slope, *b* has decreased from 85.9 to 60.4 mV per decade (average of runs 2–4). This is also clear from Fig. 7, where the slope of the curve near OCV is steeper in the case of run 1 as compared to runs 2–4. The drop in the Tafel slope indicates that the electrochemical reaction sites have become more active over a period of operation and during thermal cycling of the stack. On the other hand, the ohmic resistance, *R* has increased from 0.328 Ω cm^2 (run 1) to 0.428 Ω cm^2 (average of runs 2–4). This increase in the ohmic resistance appears to be the major cause for the stack performance degradation. The possible reasons for degradation in the electrical output of the stack are: membrane degradation, increase in the contact resistance between various stack components, some corrosion of the current collection plates, deterioration of the catalyst, carbon paper and the diffusion layer.

3.4. Commercial versus CMIT 1 kW_e stacks

A commercial 1 kW_e PEM fuel cell stack was also tested in our test facility [4]. The stack consisted of 19 cells and was operated using deionised water directly fed to the stack for

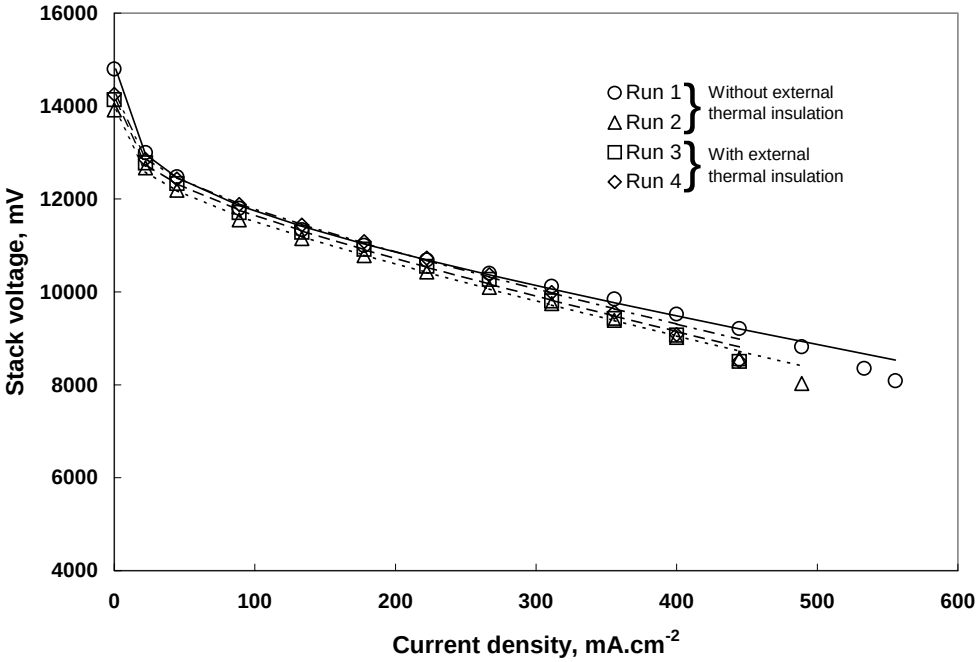

Fig. 7. *V–I* characteristics of the CMIT 1 kW_e stack operated without (runs 1 and 2) and with external thermal insulation (runs 3 and 4). The trend lines through the data points represent the fitted model (Eq. (1)). The operating parameters for different runs are given in Table 2.

humidification of gases and cooling of the stack. The commercial stack produced maximum power output of 1.02 kW_e (90 A, 11.3 V) at 64 °C as compared to 1.01 kW_e (125 A, 8.1 V) at 60 °C from the CMIT stack. Fig. 8 shows the *V–I* characteristics of the commercial stack and CMIT 1 kW_e stack. The power output of both stacks is also plotted in Fig. 8 on the secondary *Y*-axis. The *V–I* characteristics of the CMIT stack show that at 90 A, the stack voltage was 9.52 V (0.635 V average cell voltage at 0.857 kW_e stack power output). Therefore, by addition of four more cells to this stack (i.e. total 19 cells), it would produce 12.06 V at 90 A with a power output of 1.085 kW_e. The operation at a lower current density would also improve the electric efficiency of the CMIT stack.

In Table 2, the design and operating parameters of the CMIT 1 kW_e stack, commercial 1 kW_e stack and Ballard [9]

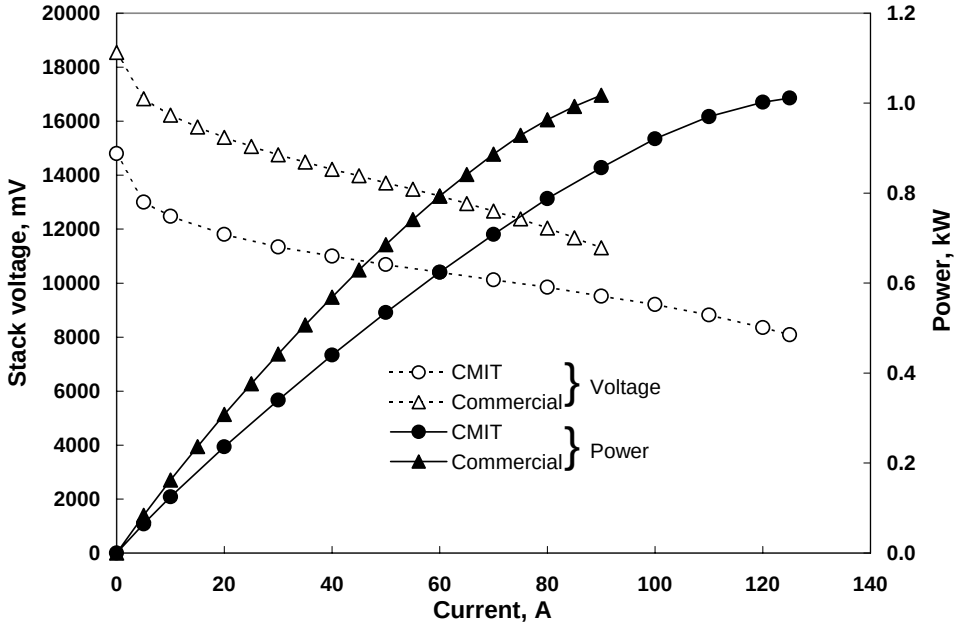

Fig. 8. Comparison of *V–I* characteristics and electric power output of CMIT 1 kW_e stack and commercial 1 kW_e stack.

5 kW_e stack have been compared. There are a number of attributes, which are common to these stacks. The electric efficiency of the stacks ranged from 39 to 45%. The heat output in the form of hot water (60–68 °C) can be captured at 35–40% efficiency, boosting the CHP efficiency of the stack to 80% as seen in Table 2 and Fig. 6. The heat output in terms of hot air exiting the stack constitutes only a small percentage, i.e. 2–4.5%, but nevertheless can form a part of the heating system for residential/commercial buildings. A 1 kW_e capacity fuel cell stack running at 45% electric efficiency can produce approximately 0.6 l h^{-1} (at stack operating temperature) of pure water that accompanies the spent air from the stack. This water can either be used for humidification of gases or can form part of the cooling water circuit, or can be used elsewhere. The heat losses from the stack, which may be somewhat difficult to harness, account for only 15–18% of the energy content of the fuel.

The model parameters determined from the *V–I* data of the three stacks are also given in Table 2. It is obvious that the Tafel slopes for all three stacks (excluding run 1 of CMIT stack) are in the range 58.2–69.1 mV per decade. The ohmic resistance, *R*, of the Ballard stack [9] was significantly lower (0.264 Ω cm^2, operating history unknown) compared to the CMIT stack (0.428 Ω cm^2 (after more than 40 cold start/shut down cycles and ∼300 h accumulated operation over a period exceeding one year), and commercial stack (0.543 Ω cm^2, less than 48 h operation). However, it is worth mentioning that CMIT 2- and 4-cell stacks had also registered lower ohmic resistance values of 0.251 and 0.228 Ω cm^2, respectively, as shown in Table 1.

4. Conclusions

A 1 kW_e PEM fuel cell stack was constructed and evaluated in stages of 2-, 4-, 8- and 15-cell. The stack produced an electric efficiency of 41% and with external thermal insulation it produced CHP efficiency of 80%. The stack showed a small degradation in its performance after undergoing more than 40 cold start/shut down thermal cycles and ∼300 h accumulated operation over a period exceeding one year as indicated by an increase in the average ohmic resistance of cells from 0.328 to 0.428 Ω cm^2. Possible causes for increase in the ohmic resistance and degradation in the electrical output of the stack are: membrane degradation, increase in the contact resistance between various stack components, some corrosion of the current collection plates, deterioration of the catalyst, carbon paper and the diffusion layer. The Tafel slope values for CMIT 1 kW_e stack, commercial 1 kW_e stack and Ballard 5 kW_e stack were in the range of 58.2–69.1 mV per decade. The ohmic resistance of the CMIT 1 kW_e stack was higher than that of the Ballard stack. However, the CMIT 2- and 4-cell stacks had registered lower ohmic resistance values of 0.251 and 0.228 Ω cm^2, respectively. Thus with appropriate design modifications and consideration to reducing contact resistance between various cell components, it is possible to reduce ohmic resistance of the stack. Other areas for improving the stack performance are modelling of air and fuel flow fields for more uniform reactant distribution and water flow fields and heat balance for more uniform stack temperature.

Acknowledgements

Authors would like to thank Viktor Zelizko and Kristine Giampietro for assistance with experimentation and Dr. Manh Hoang and Carl Mitchell for review of the manuscript.

Appendix A

Energy and mass balance equations:

$$P_{tot} = q_{H_2} \rho_{H_2} \Delta H$$

$$P_{elect} = \text{stack voltage} \times \text{stack current}$$

$$Q_w = q_w \rho_w C_{p,w} (T_{wi} - T_{wo}) c$$

$$Q_a = q_a \rho_a C_{p,a} (T_{ai} - T_{ao}) c$$

$$Q_{other} = P_{tot} - (P_{elect} + Q_w + Q_a)$$

c	conversion factor for cal h^{-1} to kW (11.628×10^{-7} kW h cal^{-1})
$C_{p,a}$	heat capacity of air (cal g^{-1} °C^{-1})
$C_{p,w}$	heat capacity of water (cal g^{-1} °C^{-1})
ΔH	enthalpy change of hydrogen (143 kJ g^{-1}) (HHV)
P_{elect}	electric energy produced by the stack (kW)
P_{tot}	total energy available from hydrogen (kW)
q_a	volumetric flow rate of air (l h^{-1})
q_{H_2}	volumetric flow rate of hydrogen (l s^{-1})
q_w	volumetric flow rate of water (ml h^{-1})
Q_a	heat gained by the air (oxidant) supplied to the stack (kW)
Q_{other}	other heat losses from the stack, mainly due to heat exchange with the surroundings (kW)
Q_w	heat gained by the cooling water supplied to the stack (kW)
T_{ai}	inlet temperature of air (°C)
T_{ao}	outlet temperature of air (°C)
T_{wi}	inlet temperature of cooling water (°C)
T_{wo}	outlet temperature of cooling water (°C)
ρ_a	density of air (g l^{-1})
ρ_{H_2}	density of hydrogen (0.0833 g l^{-1})
ρ_w	density of water (g ml^{-1})

References

[1] S.P.S. Badwal, in: B.V.R. Chowdari, K. Lal, S.A. Agnihotri, N. Khare, S.S. Sekhon, P.C. Srivastava, S. Chandra (Eds.), Solid State Ionics: Science and Technology, World Scientific, Singapore, 1998, p. 567.

[2] A.U. Dufour, J. Power Sources 71 (1998) 19.
[3] M. Uchida, Y. Fukuoka, Y. Sugawara, H. Ohara, A. Ohta, J. Electrochem. Soc. 145 (1998) 3708.
[4] E. Passalacqua, F. Lufrano, G. Squadrito, A. Patti, L. Giorgi, Elecrochim. Acta 43 (1998) 3665.
[5] V.A. Paganin, E.A. Ticianelli, E.R. Gonzalez, J. Appl. Electrochem. 26 (1996) 297.
[6] S. Giddey, F.T. Ciacchi, S.P.S. Badwal, V. Zelizko, J.H. Edwards, G.J. Duffy, Solid State Ionics 152–153 (2002) 363.
[7] J.C. Amphlett, R.M. Baumert, R.F. Mann, B.A. Peppley, P.R. Roberge, J. Electrochem. Soc. 142 (1995) 1.
[8] J. Kim, S. Lee, S. Srinivasan, J. Electrochem. Soc. 142 (1995) 2670.
[9] F. Laurencelle, R. Chahine, J. Hamelin, K. Agbossou, M. Fournier, T.K. Bose, A. Laperrière, Fuel Cells 1 (2001) 66.
[10] D. Chu, R. Jiang, J. Power Sources 83 (1999) 128.